INTERNATIONAL JOURNAL OF HYDROGEN ENERGY 43 (2018) 15659–15672

Available online at www.sciencedirect.com

ScienceDirect

journal homepage: www.elsevier.com/locate/he

Two-phase flow behaviour and performance of polymer electrolyte membrane electrolysers: Electrochemical and optical characterisation

Jude O. Majasan [a], *Jason I.S. Cho* [a,b], *Ishanka Dedigama* [a], *Dimitrios Tsaoulidis* [a], *Paul Shearing* [a], *Dan J.L. Brett* [a,*]

[a] *Electrochemical Innovation Lab, Department of Chemical Engineering, University College London, London, WC1E 7JE, UK*

[b] *Centre for Nature Inspired Engineering, Department of Chemical Engineering, University College London, London, WC1E 7JE, UK*

ARTICLE INFO

Article history:
Received 10 February 2018
Received in revised form
27 June 2018
Accepted 1 July 2018
Available online 24 July 2018

Keywords:
Polymer electrolyte water electrolyser
Flow-field
Gas-bubble dynamics
Two-phase flow
High-speed optical visualization

ABSTRACT

Understanding gas evolution and two-phase flow behaviour are critical for performance optimization of polymer electrolyte membrane water electrolysers (PEMWEs), particularly at high current densities. This study investigates the gas-bubble dynamics and two-phase flow behaviour in the anode flow-field of a PEMWE under different operating conditions using high-speed optical imaging and relates the results to the electrochemical performance. Two types of anode flow-field designs were investigated, the single serpentine flow-field (SSFF) and parallel flow-field (PFF). The results show that the PFF design yielded a higher cell performance than the SSFF design at identical operating conditions. Optical visualization shows a strong relationship between the flow path length and the length of gas slugs produced, which in turn influences the flow regime of operation. Longer flow path length in the SSFF results in annular flow regime at a high current density which degrades cell performance. The annular flow regime was absent in the PFF design. It was found the effect of flow rate on performance depends strongly on operating temperature in both flow patterns. Results of this study indicate that long channel length promotes gas accumulation and channel-blocking which degrades performance in PEMWEs.

Introduction

With the growing concerns over energy efficiency and environmental sustainability, renewable energy sources such as solar and wind are becoming increasingly attractive and gaining widespread use [1–5]. However, a major challenge limiting their practical application is their intermittent power production. Therefore, large-scale renewable energy deployment depends greatly on the development of efficient and economical energy storage systems [5]. The polymer electrolyte membrane water electrolyser (PEMWE), is regarded as a promising candidate for large-scale renewable energy storage and green hydrogen production [5–7]. It possesses several advantages over the conventional alkaline electrolysers,

* *Corresponding author.*
E-mail address: d.brett@ucl.ac.uk (D.J.L. Brett).

https://doi.org/10.1016/j.ijhydene.2018.07.003

including reduced gas crossover, higher conversion efficiency, fewer corrosion issues, more compact construction and operation over a wider range of current densities. For these reasons, research interest in PEMWE has intensified in recent years [8–19].

Despite the advantages of the PEMWE technology, its large-scale commercialization is hampered by critical issues associated with performance, durability and cost. To reduce investment cost and increase the diversity of use (particularly for wind and solar applications) operation at high current densities, with good efficiency, is desirable [17,20]. At high current densities, large amounts of gas are formed, which presents a challenge for removing the product and ensuring that the electrodes receive an adequate supply of water. Accumulation of O_2 gas can act to shield the anode from water and different two-phase flow regimes can exist that will affect the mass transport of both water and the produced gas. The resultant electrolyser performance is determined by the complex interplay of mass and charge transfer, heat and electrochemical factors, all of which are affected by the flow-field design, current density, temperature and water flow rate.

Despite its great importance when operating at high current density, relatively little research has focused on the link between two-phase flow characteristics and electrochemical performance of PEMWEs. Ito et al. [21] studied different flow-field designs and examined the effects of current density, water flow rate and cell temperature and found that mass transport limitations are more pronounced in the slug or annular regime than in the bubbly regime and that there is a strong relationship between the two-phase flow regime and performance. Dedigama et al. [22,23] studied the two-phase flow characteristics as a function of current density and water flow rates using high-speed imaging in the anode flow-field of a transparent PEMWE equipped with a parallel flow-field. They also investigated the heat distribution and current density distribution across the active area of the cell. Results showed how the flow regime evolves along a channel from bubbly to slug/annular and that this is associated with an increase in local current density towards the end of a channel. Lafmejani et al. [24] studied the pattern of vertical upward gas-liquid flow in a single straight channel by optical visualization in an ex-situ setup. They analysed two-phase flow phenomena in PEMWE by gas injection through a permeable wall made of titanium felt into a transparent channel of flowing water. Their result indicated that bubble coalescence occurred along the channel length and bubbly-flow, Taylor flow and annular flow regimes were observed. Selamet et al. [25] combined neutron radiography with optical imaging to examine gas evolution at the anode and cathode sides of an operational PEMWE. Using the evolution of water thickness with time, they found that gas-bubble evolution and detachment follows a cycle of periodic growth and removal of small bubble followed by prolonged blockage by large stagnant bubbles. They also investigated the effect of operating parameters and found that water flow rate, current density and operating temperatures have a significant influence on two-phase flow phenomena in PEMWE. Hoeh et al. [26] used neutron imaging to quantify gas evolution in the anode channel at various current densities and water flow rates. They found that gas void fraction in the channel decreases with increasing water flow rate and increases with increasing current density. To analyse gas evolution into the channels, Hoeh et al. [27] also investigated gas discharge into the anode flow channels using synchrotron X-ray radiography. Their results showed that there exist selective pathways for gas evolution from the liquid/gas diffusion layer and the number of such pathways increases with increase in current density.

Also, several studies have employed modelling and numerical techniques to improve understanding of two-phase flow and flow-field design in the PEM electrolyser. Nie et al. [28] performed three-dimensional numerical simulations and experimental measurements of fluid flow in a simplified bipolar plate of a PEM electrolysis cell. Their investigations in the bipolar plate with parallel flow channels showed that the pressure decreases from inlet to outlet in the diagonal direction. They also reported non-uniform distribution of velocity and temperature over the flow field. Tijani et al. [29] investigated several flow plate designs using numerical simulation to evaluate hydrodynamic properties, velocity fields and pressure gradients in different designs. Aubras et al. [30] developed a two-dimensional model for evaluation of heat and mass transfer at the PEM electrolyser electrodes taking into account two bubbly flow regimes. They suggested that the bubble coalescence phenomenon is associated with improved mass transfer and reduced ohmic resistance in the PEM electrolyser. Ruiz et al. [31] developed a mathematical and numerical framework for the investigation of the effect of flow channel configurations in a high temperature PEM electrolyser. They investigated the parallel, serpentine and multiple-serpentine flow channel configurations and suggested that the multiple-serpentine design performs better in terms of hydrogen production, temperature uniformity and pressure drop. More recently, Toghyani et al. [32] developed a three-dimensional numerical analysis for performance comparison of five flow field patterns evaluating performance based on molar fraction of produced hydrogen, current density, and temperature and their result revealed better distribution of temperature and current density in the serpentine flow field configuration.

Similar to the two-phase flow phenomena at the anode of a PEM electrolyser, the anode of a direct methanol fuel cell (DMFC) has simultaneous transport of liquid methanol reactant and evolution of CO_2 gas produced at the electrocatalyst surface. Thus, the produced CO_2 gas becomes entrained in the liquid methanol reactant, and a two-phase flow arises in the flow-field channels at the DMFC anode. Several studies have investigated the gas evolution and two-phase flow phenomena in DMFCs in relation to cell performance. Various flow-field designs have been explored including parallel, serpentine, interdigitated, grid, spiral and fractal flow-fields [33–38]. These studies have reported that the serpentine flow pattern provides the best performance due to the higher velocity, which contributes to increased convective flux and leads to better mass transport at high current densities. A few studies have investigated the effect of geometric parameters such as channel width, rib width and channel dimension ratios, among others [39–41]. Several studies have also probed bubble evolution and two-phase phenomena in DMFCs, specifically using visualization techniques [38,40,42–44]. These

studies highlight that cell performance is affected by several factors including flow-field design, channel geometry and operating parameters.

This literature review suggests that gas-bubble evolution, two-phase flow behaviour and flow-field design are closely linked to the performance of PEMWEs. However, the majority of previous PEMWE studies were performed at relatively low current densities or have analysed two-phase flow in a single straight channel where the two-phase flow pattern may not be fully representative. Others have modelled flow using flow regime maps rather than real-time flow visualization. Thus, an in-depth study of entire flow-fields that correlates design and real-time two-phase flow phenomena with performance at high current densities is desirable. Also, understanding the effect of operating parameters such as temperature, flow circulation at anode only or at both electrodes (full circulation) and water flow rate on the two-phase flow behaviour at high current densities is essential for design and performance optimization.

In this study, the two-phase flow behaviour in a PEMWE equipped with two different anode flow-field designs (serpentine and parallel) is examined and related to the electrochemical performance. By using transparent endplates, direct visual inspection of the flow channels across the whole flow-field allowed the gas-bubble dynamics and the two-phase flow behaviour to be recorded using a high-speed video camera at current densities up to 3.3 A cm^{-2}. Polarization curves were obtained to provide a fundamental understanding of the relationship between the two-phase flow behaviour and cell performance. The effects of various operating parameters including flow circulation at anode only or full circulation, water flow rate, and cell operating temperature were also investigated.

Experimental

Transparent cell design

The transparent PEMWE cell used for this study was designed and fabricated in-house and is shown schematically in Fig. 1. The MEA used was supplied by ITM Power, UK and has an active area of 3.0 × 3.0 cm^2. It consists of a Nafion 115 membrane and two electrodes with the anode composed of iridium/ruthenium oxide at a loading of 3 mg cm^{-2} and the cathode composed of platinum black at a loading of 0.6 mg cm^{-2}. The dry MEA supplied was activated by: (i) boiling in deionized (DI) water for 18 h at 60 °C; (ii) rinsing in DI water for 3 h; and (iii) in-situ activation by operating in a cell at current density of 0.1 A cm^{-2} for a period of 18 h. The MEA was sandwiched between two liquid/gas diffusion layers (LGDLs) which were sealed with PTFE gaskets to prevent leakage. The MEA and LGDLs were inserted between the anode and cathode flow-field plates that were designed in-house with the aid of CAD/CAM software (Rhino 4.0) and a CNC machine (Roland MDX 40). The entire assembly was then clamped between the two transparent end-plates using eight M5 screw joints; each tightened to a torque of 1.5 Nm. Transparent PVC gaskets of

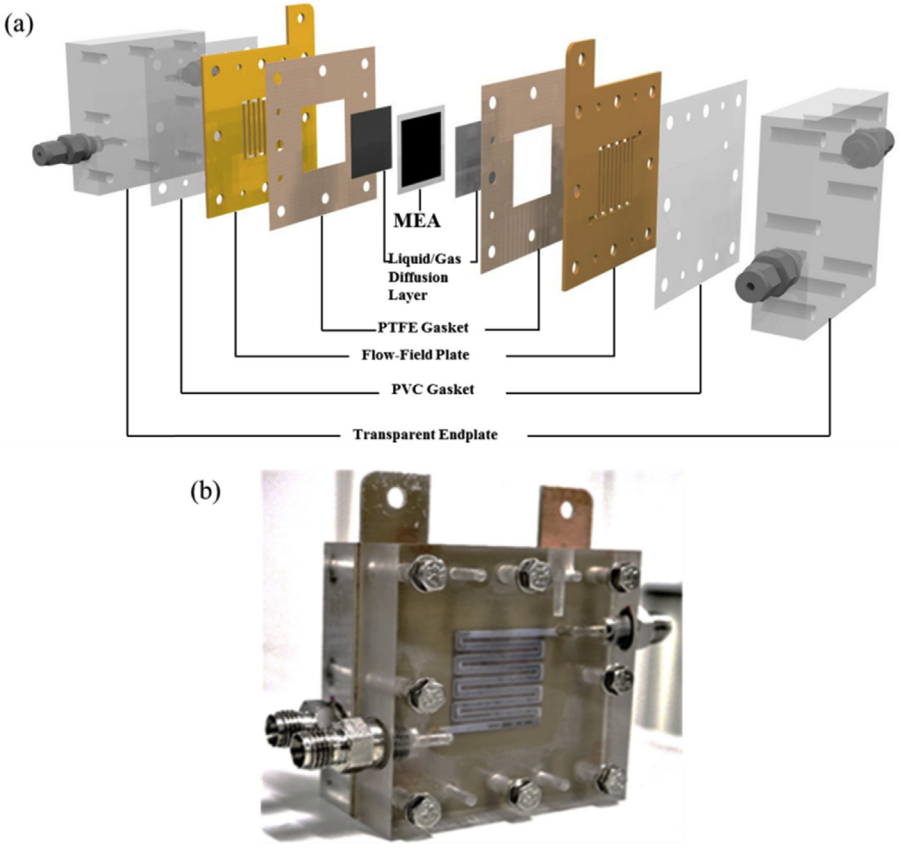

Fig. 1 – In-house fabricated transparent PEMWE: (a) schematic of cell components; (b) photograph of the assembled cell.

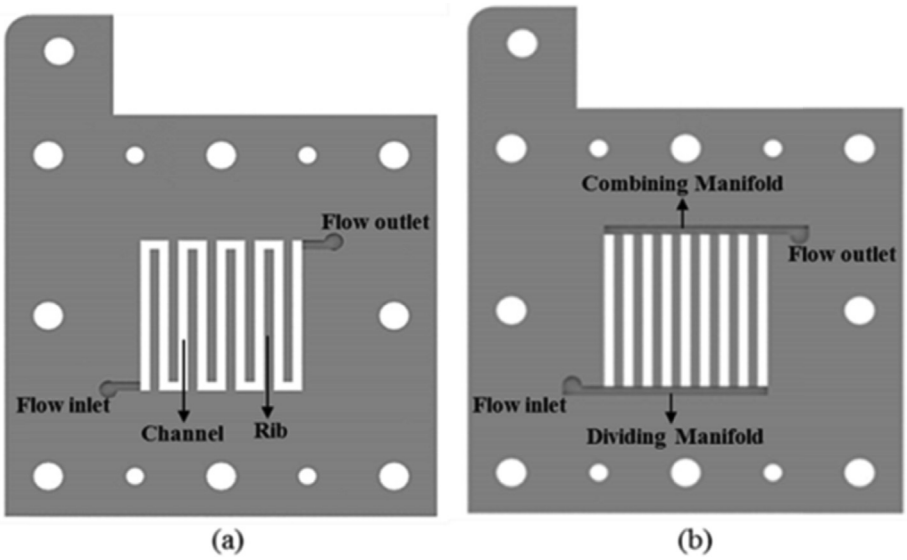

Fig. 2 – Flow-field plate designs, (a) single-serpentine flow-field (SSFF), (b) parallel flow-field (PFF).

thickness 0.19 mm were placed between the flow-field plates and the end-plates to prevent water leakage.

Both the cathode and anode flow-field plates were machined from a 1.6 mm-thick printed circuit board (PCB) material, which consists of an FR4 board clad with a 35 μm-thick copper layer. The copper layer was electroplated with a 12 μm-thick nickel layer and a 5 μm-thick gold layer to provide good conductivity and corrosion resistance. Titanium sinter having thickness 0.35 mm was used as the anode LGDL and a 0.19 mm-thick unteflonated carbon paper TGP-H-060 (Toray, Inc.) was used as the cathode LGDL. The two end-plates were made of 20 mm-thick transparent polymethyl methacrylate (PMMA) material to allow optical access for gas-bubble and two-phase flow characterization.

Fig. 2 shows the two anode flow-field designs used in this study. Fig. 2(a) illustrates the single serpentine flow-field (SSFF), and Fig. 2(b) illustrates the parallel flow-field (PFF). As shown, the SSFF consisted of a single meandering flow channel having nine linked vertical segments (each 30 mm long) and eight horizontal segments (each 1.76 mm long), whereas the PFF comprised nine parallel straight channels, each 30 mm long. Both flow-field designs have channel depth of 1.6 mm and a channel and rib width of 1.76 mm to maintain the same open ratio (ratio of channel area to MEA area) of 55.7% and provide a basis for comparison. At the cathode side, a single serpentine flow-field with 1.76 mm channel width and rib width and 1.6 mm depth was used for all the experiments in this study.

A 'diagonal flow mode' was adopted in both of the flow-field designs such that the water was fed to the flow-field from the lower left corner (as shown in Fig. 2) while excess water and the gas produced was ejected at the upper right corner. While the SSFF does not require a manifold and there is no flow branching, the PFF incorporates a dividing manifold at the bottom of the flow-field and a combining manifold at the top (Fig. 2(b)). Both manifolds had the same channel dimensions as the main flow channels. In the case of the PFF, the 'diagonal flow mode' is equivalent to a Z-type manifold configuration. As opposed to the U-type (where the outlet is on the same side as inlet), for uniformly sized conduits Z-type manifolding usually results in more uniform flow and pressure drop for fuel cells, electrolysers and cooling plates [45].

Test rig

The setup of the experimental test rig is shown in Fig. 3. DI water was supplied from a water reservoir to the PEMWE cell by a digital peristaltic pump (Watson Marlow 323U). The cell was operated at ambient pressure and heated to the desired temperature by preheating the inflowing deionized water supplied to both the anode and cathode side of the cell using a digital heated circulating bath (TC120, Grant Instruments Ltd). Three inlet water temperatures were used in this study: 25 °C, 45 °C, and 80 °C. Excess unreacted water and product O_2 and H_2 gas are returned to the water reservoir where the gases are separated and vented while the DI water is recycled to the cell. The cell was orientated vertically in all the experiments.

Electrochemical measurement

The voltage–current polarization curves (V–i curves) were obtained using Gamry Reference 3000 Galvanostat/Potentiostat equipped with a Gamry 30k Booster (Gamry Instruments, USA). The data were acquired using the Gamry Framework software (version 6.24) on the potentiostat. In the polarization curve measurements, the cell electrolysis voltage was measured as the applied current was increased stepwise, at a scan rate of 0.1 A s^{-1} from 0.1 A to 30 A. Initial steady-state operation was ensured before all polarization curve measurement by applying an initial load of 0.1 A cm^{-2} to the cell for 15 min. A constant potential was attained within this time period, indicating the stability of the electrode. Three or more voltage-current polarization curves were run at all conditions investigated to test repeatability. The cell performance was repeatable to within 10% and all the trends in cell performance was preserved.

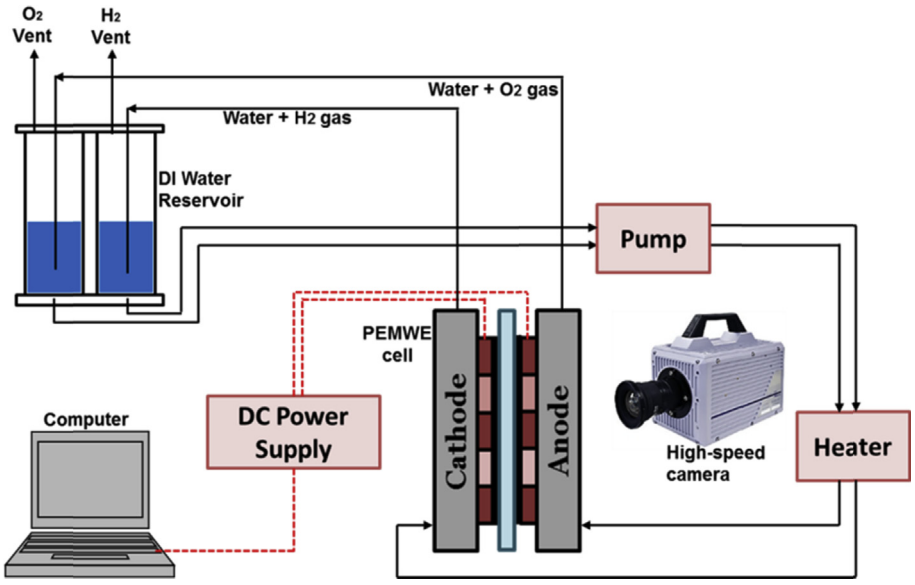

Fig. 3 – Schematic diagram of experimental setup for the simultaneous visualization and electrochemical study.

Image recording system

A CMOS high-speed imaging system (Phantom V1212, Monochrome) with a maximum resolution of 1280 × 800 pixels was employed to acquire continuous 10-bit images of the bubble evolution and two-phase flow behaviour of O_2 gas and water in the anode flow channel at 1000 frames per seconds. The anode channel was illuminated with an 84 W high-power LED lighting system (Photo-Sonics Ltd). The images were digitally evaluated using Phantom Camera Control (PCC, version v2.14.727.0.) software. The anode flow-field of the PEMWE cell was visualized in-situ at current densities ranging from 0.1 A cm^{-2} to 3.3 A cm^{-2}; three operating temperatures of 25 °C, 45 °C, and 80 °C; and four different water flow rates of 15, 30, 45 and 60 ml min^{-1}. The flow velocity was determined by tracking the movement of bubble/slug from consecutive images based on the time interval (number of frames) for the bubble/slug to travel a given distance.

Feed water flow rate

A minimum amount of liquid water is required to sustain the reaction at the electrolyser anode; this depends on the current density of operation. The molar rate of water consumption for the anode reaction $\dot{N}$ is given by Faraday's Law:

$$\dot{N} = \frac{iA}{2F} \quad (1)$$

where i is the current density, A is the active area of the electrode, and F is Faraday's constant (96485.3 C mol^{-1}). The ratio (ξ) of inlet water flow rate to the amount of water needed for the anode electrolysis reaction for a single cell can be calculated according to Eq. (2):

$$\xi = \frac{G_{circ}}{G_{cons} + G_{drag}} \quad (2)$$

where G_{circ} is the mass flux of inlet feed water, G_{cons} is the mass flux of water consumed by the anode reaction and G_{drag} is the mass flux of water transported to the cathode side by electroosmotic drag, and is estimated to be about 10 times that of G_{cons} [21]. Notionally, a value of $\xi = 1$ is sufficient to sustain the electrolysis reaction at the anode. However, a value of $\xi = 5$ is typical in actual operation of large cells or stacks to prevent electrode starvation or membrane dehydration [9]. Based on calculations using Eq. (2), for the range of current density and inlet water flow rates used in this study, ξ ranges between 7.5 at 3 A cm^{-2} when operated at 15 ml min^{-1} and 30 when operated at 60 ml min^{-1}. This implies that the water flow rates (15, 30, 45 and 60 ml min^{-1}) used are always in significant stoichiometric excess and sufficient to keep the MEA well hydrated throughout the electrolysis operation.

Results and discussion

General features of gas-bubble dynamics in the anode flow-field of the PEMWE

Before examining the specific features of different flow-field designs and operating conditions (Figs. 4–6 and 8 and 9), it is useful to consider certain generic features of the bubble distribution and flow characteristics in the flow channels. In general, the lighter areas in the images represent single-phase liquid flow and areas containing small bubbles; whereas the darker areas correspond to larger bubbles or slug flow, through which the dark LGDL/electrode becomes visible through the gas phase. The change in shape, size and flow regimes of gas bubbles with an increase in current density for any single channel has the following general trend. At very low current density, numerous small, spherically-shaped gas bubbles emerge from various locations on the LGDL surface and remain attached due to surface tension forces. The gas bubbles become detached when the dynamic pressure of the flowing water exceeds the surface adhesion force and the gas bubbles join the flow of water. Initially, the bubbles are

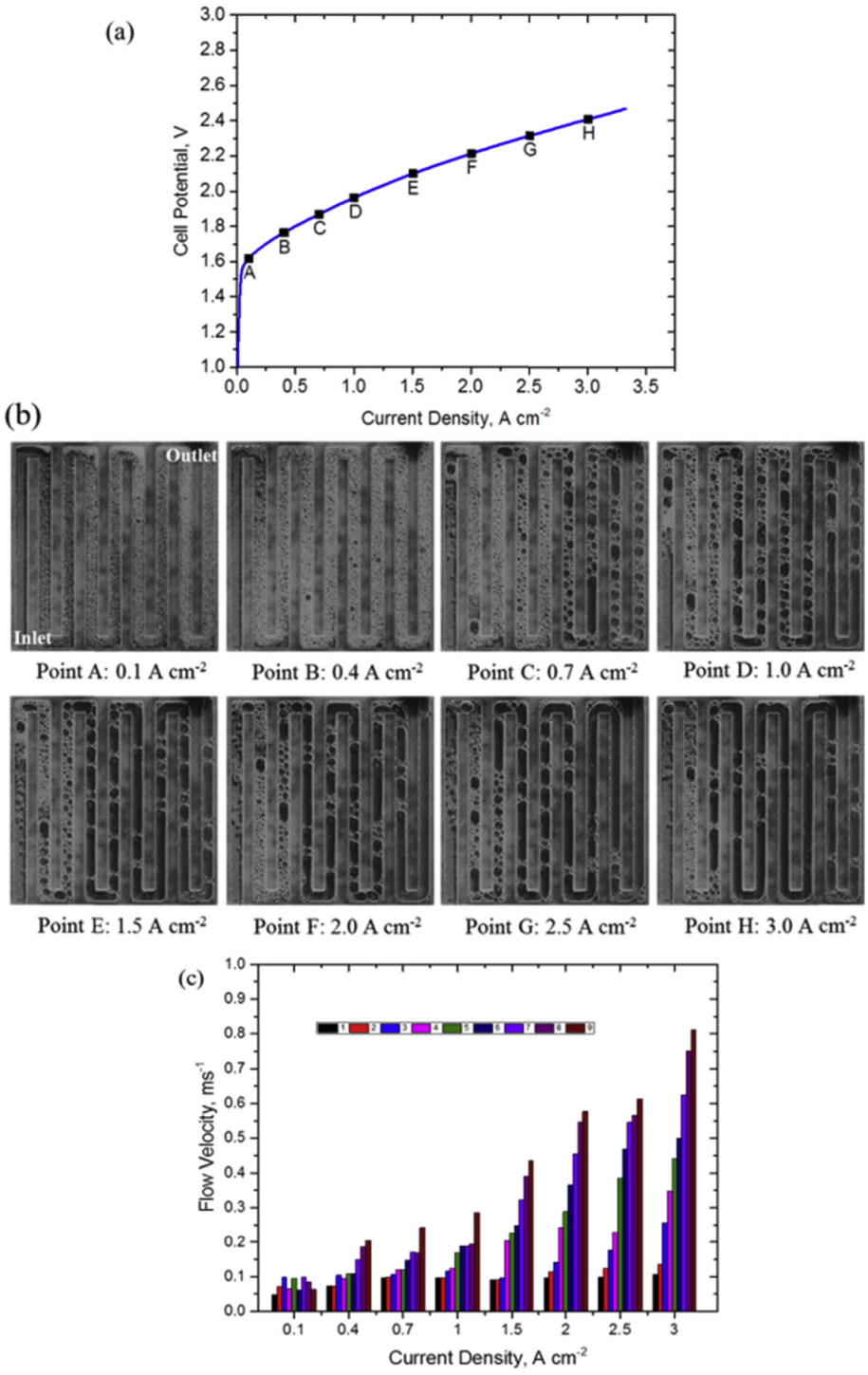

Fig. 4 – (a) Polarization curve for SSFF design at a temperature of 80 °C and feed water flow rate of 15 ml min^{-1}; (b) O_2 gas-bubble behaviour at selected current densities; and (c) flow velocity profile in sub-channels 1 to 9 of the SSFF at various current densities.

dispersed in the flow of liquid water, characterised by the bubbly-flow regime. As current increases and more gas is produced, and/or as the bubbles depart and coalesce with newly formed bubbles further along the channel, transition to the slug flow regime occurs. This regime is characterized by elongated 'cylindrical' bubbles also known as Taylor bubbles, whose lengths are several times larger than the width of the channel. As more gas is produced with further increase in current density, the gas void fraction increases and strings of Taylor bubbles separated from one another by clusters of small bubbles move along the channel. The slug flow, in which bubbles fill the majority of the channel cross-section, with only a thin boundary layer of water at the edges, has a 'sweeping' effect on the nascent bubbles forming at the

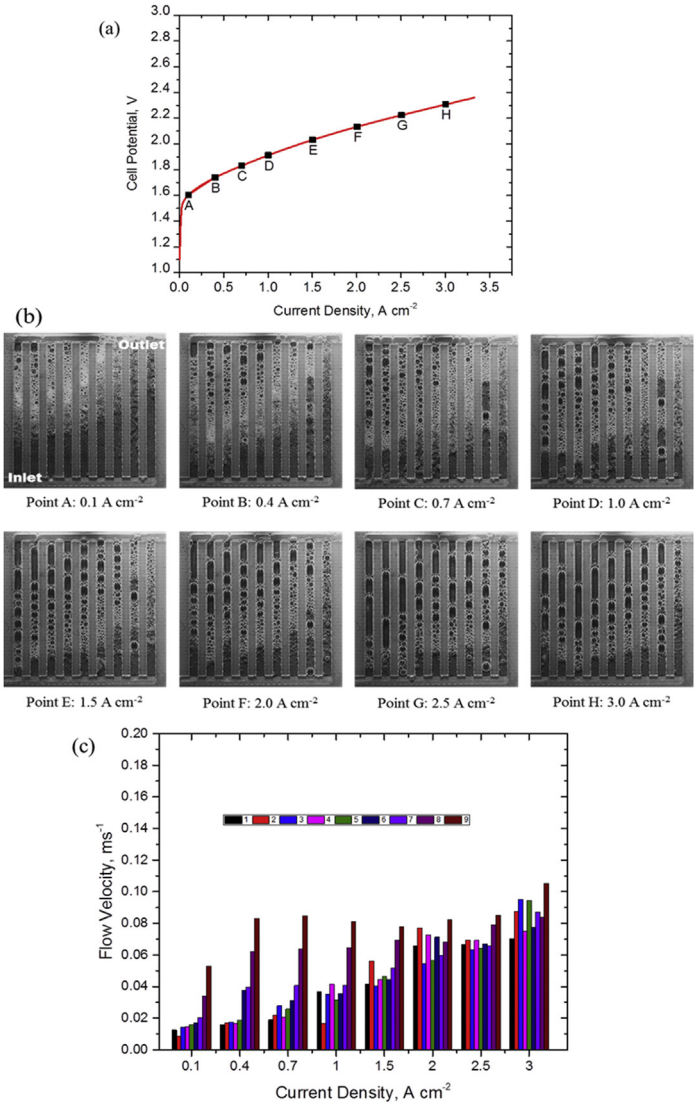

Fig. 5 – (a) Polarization curve for PFF design at a temperature of 80 °C and feed water flow rate of 15 ml min^{-1}; (b) anode two-phase flow behaviour at selected current densities; and (c) flow velocity in the PFF channels 1–9 at various current densities.

surface of the LGDL, and acts to clear the channel along the downstream region. As will be shown below, in a flow-field with extended channel length (the SSFF in our case), as more gas is produced at high current densities, the two-phase flow enters a regime known as annular flow, where most of the liquid flows along the channel walls as the central channel core is dominated by long gas slugs. The process of bubble emergence, growth, detachment, coalescence and eventual sweeping by slug or annular flow was a feature observed across the range of flow-field designs and operating conditions examined.

Two-phase flow behaviour in the Single Serpentine Flow-Field (SSFF)

Fig. 4(a) shows the cell polarization curve obtained for the SSFF operated at a temperature of 80 °C and inlet water flow rate of 15 ml min^{-1}. Fig. 4(b) shows the images of the SSFF at selected current densities corresponding to Point A to H in Fig. 4(a). The images show that the total amount of gas present in the flow channel increases continuously with increase in current density.

At very low current density of 0.1 A cm^{-2}, corresponding to point A, numerous tiny bubbles were observed in the flow channel. Then, as current density increased to 0.4 A cm^{-2}, corresponding to point B, the quantity and size of the gas bubbles increased significantly due to increased gas generation and bubble coalescence, and the flow pattern observed is described as the bubbly regime. As current density increased to 0.7 A cm^{-2} (Point C), gas fraction and bubble coalescence along the channel length increased leading to the formation of larger spherical bubbles and emergence of short cylindrical gas slugs along the channel downstream. The short gas slugs coexist with the smaller bubbles present and the flow pattern observed is described as an intermediate between the bubbly and slug regime. Also, along with the emergence of slugs, the flow velocity starts to increase for each sub-channel. As current density increased to 1.0 and 1.5 A cm^{-2}, corresponding to point D and E, longer gas slugs are formed accompanied by a

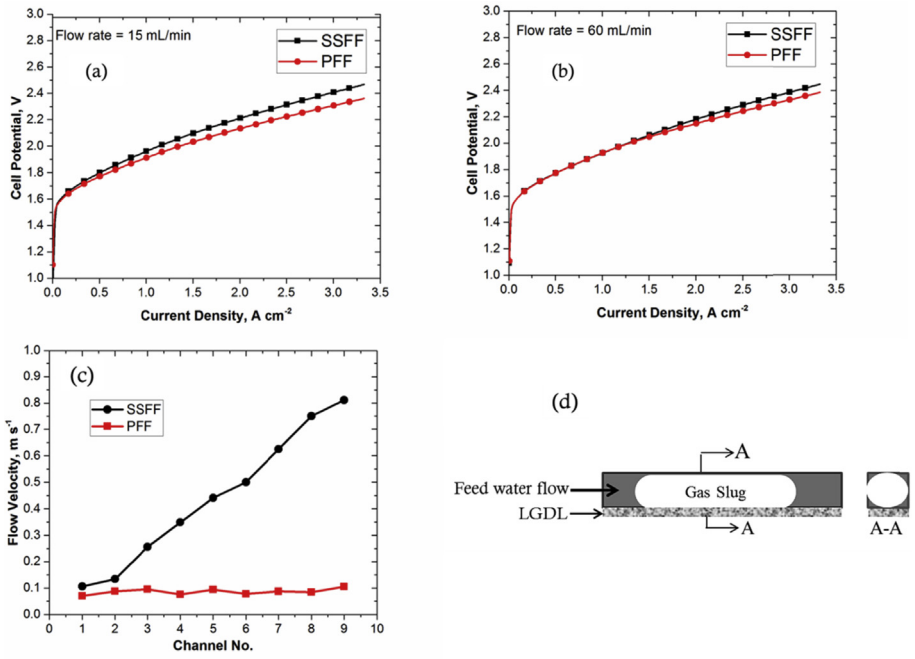

Fig. 6 – Performance curve of PEM electrolyser equipped with different flow-fields at water flow rates of (a) 15 ml min^{-1} and (b) 60 ml min^{-1} at an inlet water temperature of 80 °C; (c) comparison of flow velocity in the flow channels for the two flow-field designs at 3 A cm^{-2} at an inlet water flow rate of 15 ml min^{-1}; (d) illustrated model of gas slug in flow-field channel showing the probable LGDL-blocking action.

corresponding increase in flow velocity. At these current densities, the flow channel is observed to be divided into two regions, the downstream dominated by pockets of long cylindrical gas slugs separated by spherical gas bubbles, and the upstream region filled with relatively smaller gas bubbles. At the high current densities of 2.0, 2.5 and 3.0 A cm^{-2}, corresponding to points F, G and H, respectively, the gas slug grows rapidly along the meander as the smaller bubbles coalesce earlier along the channel. Thus, at these high current densities, a larger portion of the flow channel is filled with continuous meandering gas slugs (annular regime). At an average current density of 3 A cm^{-2} (Point H), about 80% of the flow channel is filled with continuously meandering gas slugs; as only the two sub-channels closest to the channel inlet are free of slugs.

It is worth mentioning that a prominent feature of the two-phase flow in the SSFF is that the channel corners (switch-backs) were convenient locations for the coalescence of gas bubbles/slugs. Gas bubbles and slugs were more likely to coalesce when they go around the corners, which might have significant implication for the transition between flow regimes.

The flow velocity in each of the nine sub-channels of the SSFF design is presented in Fig. 4(c). The flow velocity was determined by tracking the movement of bubble/slug from consecutive images based on the time interval (number of frames) for the bubble/slug to travel a given distance. It can be seen that at a given current density, the velocity increases along the length of the meander from the inlet to the outlet. The lowest velocity was recorded in the sub-channel closest to the inlet (sub-channel 1) and the highest velocity recorded in the sub-channel closest to the outlet (sub-channel 9) for each current density considered. Also, the increase in flow velocity across the flow-field was observed to correspond to slug formation. As gas bubbles accumulate and coalesce along the channel length, the void fraction of the gas-phase thus increases with channel length and consequently slugs are formed along the channel downstream. The increased gas void fraction and slug formation towards the channel downstream thus lead to decrease in the cross-sectional area of the liquid-phase flow which increases the flow velocity.

Two-phase flow in parallel flow-field (PFF)

Fig. 5(a) shows the cell polarization curve obtained for the PFF operated at a temperature of 80 °C and feed water flow rate of 15 ml min^{-1}. Fig. 5(b) illustrates the corresponding images of the two-phase flow behaviour at selected current densities on the polarization curve, which correspond to Point A to H in Fig. 5(a).

It can be seen from Fig. 5(b) that in the PFF, the quantity of gas and hence the size of gas bubbles, increased with current density, consistent with the observations in Fig. 4(b). Depending on the current density, for any given channel there is the trend for the flow regime to evolve as described above for the SSFF. However, the PFF shows a non-uniform distribution of flow between the channels. The liquid flow rate was highest in the channel farthest from the inlet and lowest in the channel closest to the inlet. This is attributed to the well-known inertial effect of fluid flow out from a dividing manifold into multiple T-junctions, which makes the fluid prefer the straight direction (horizontally along the manifold) rather than branching (vertically into the channels) [45]. This has an

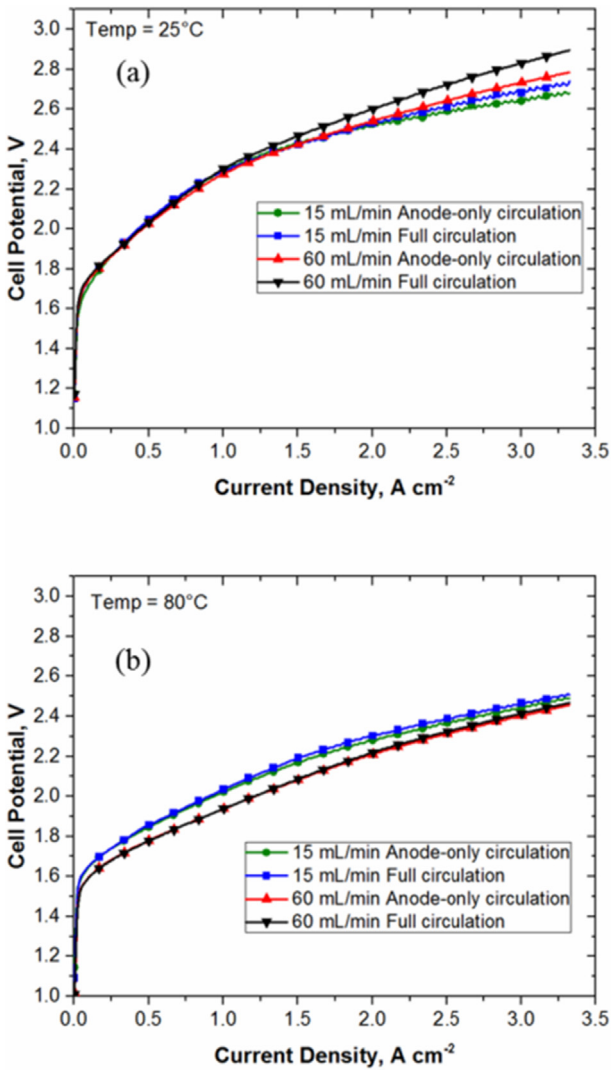

Fig. 7 – Effect of feed water circulation on performance at (a) 25 °C and (b) 80 °C using the PFF design at the cell anode and water flow rates of 15 ml min^{-1} and 60 ml min^{-1}.

important effect on the resultant two-phase flow evolution in each of the channels.

At low current density of 0.1 A cm^{-2}, corresponding to Point A in Fig. 5(a), the lower portion of the channels are filled with liquid water with the upper portion consisting mainly of gas bubbles with width smaller than the channel cross-section. It can be seen that the quantity of bubbles in the channels varies, with the channel closest to the inlet having a large quantity of tiny bubbles whereas the channels furthest from the inlet have a significantly smaller amount of bubbles due to the higher flow velocity and consequent lower gas volume fraction. This trend was observed at all current densities considered for flow visualization and is attributed to non-uniform distribution of flow in the channels. As current density increased to 0.4 A cm^{-2} (point B), both the quantity and size of the gas bubbles have increased markedly, with increase to 0.7 A cm^{-2} (Point C) bubble coalescence leads to emergence of short gas slugs in the channels closest to the cell inlet while the other channels remain noticeably bubbly. As the average current density increased to 1.0 and 1.5 A cm^{-2}, corresponding to point D and E, short gas slugs begin to form in the middle channels, while the early-appearing gas slugs in the channels closest to the inlet begin to lengthen and move downstream. A similar trend was observed at higher current densities of 2.0, 2.5 and 3.0 A cm^{-2} corresponding to points F, G and H respectively. Further gas generation and bubble coalescence led to the formation of gas slugs in the channels farther away from the inlet, and at 3.0 A cm^{-2}, only the two channels furthest away from the inlet remain exclusively bubbly. The overall trend in this flow-field pattern is a transition from bubbly to slug regime and occurs at progressively longer times as the channels move away from the manifold inlet.

Notably, the transition to gas slugs spanning entire flow channels (annular regime) did not occur in this flow-field configuration because the gas slugs enter the combining manifold before this transition could occur. Fig. 5(c) shows the flow velocity in the PFF channels corresponding to various current densities tested at an inlet water flow rate of 15 ml min^{-1}. It can be seen that the flow velocity increased approximately linearly (within the error of flow velocity measurements) with average current density (ranging from a flow velocity of 0.02 m s^{-1} at 0.1 A cm^{-2}, to 0.09 m s^{-1} at 3 A cm^{-2}), which is consistent with a linear increase in gas generation (gas void fraction) and constant water inlet flow. However, the distribution of flow velocities across the nine channels changes, becoming increasingly uniform with increasing current density. Numerous factors will affect this flow distribution, the two-phase flow state of the combining manifold being one of them, but in general gas-filled channels (higher gas void fraction) will present a lower pressure drop (i.e. channels towards the water intake), thus acting to balance the flow velocity into each channel. It should be noted that, the theoretical flow velocity, assuming single-phase water flow through the channels equally, is calculated to be 0.01 m s^{-1}, which implies that, as expected, the presence of gas increases the flow velocity in the channels at the current densities considered.

Performance comparison in serpentine and parallel flow-field designs

Fig. 6 compares the performance of the PFF and SSFF designs. The experiments were performed at two water flow rates (15 ml min^{-1} and 60 ml min^{-1}) and a fixed inlet water temperature of 80 °C. It is clear from Fig. 6(a) and (b) that for the same water flow rate the PFF showed better performance than the SSFF, especially at higher current densities. For instance, at 3 A cm^{-2} for water flow rate of 15 ml min^{-1}, the PFF performed better by about 100 mV compared to the SSFF. The improved performance observed in the parallel flow-field design compared to the single serpentine flow field has also been reported in previous work by Ito et al. [21]. To explain this observation, we compare the performance (polarization) curve results with the flow visualization results presented in Section General features of gas-bubble dynamics in the anode flow-field of the PEMWE. Two key differences can be observed in the visualization results of the two flow designs. First, the flow velocity in the two designs differs markedly (Fig. 6(c)). The flow velocity is significantly higher in the SSFF than in the

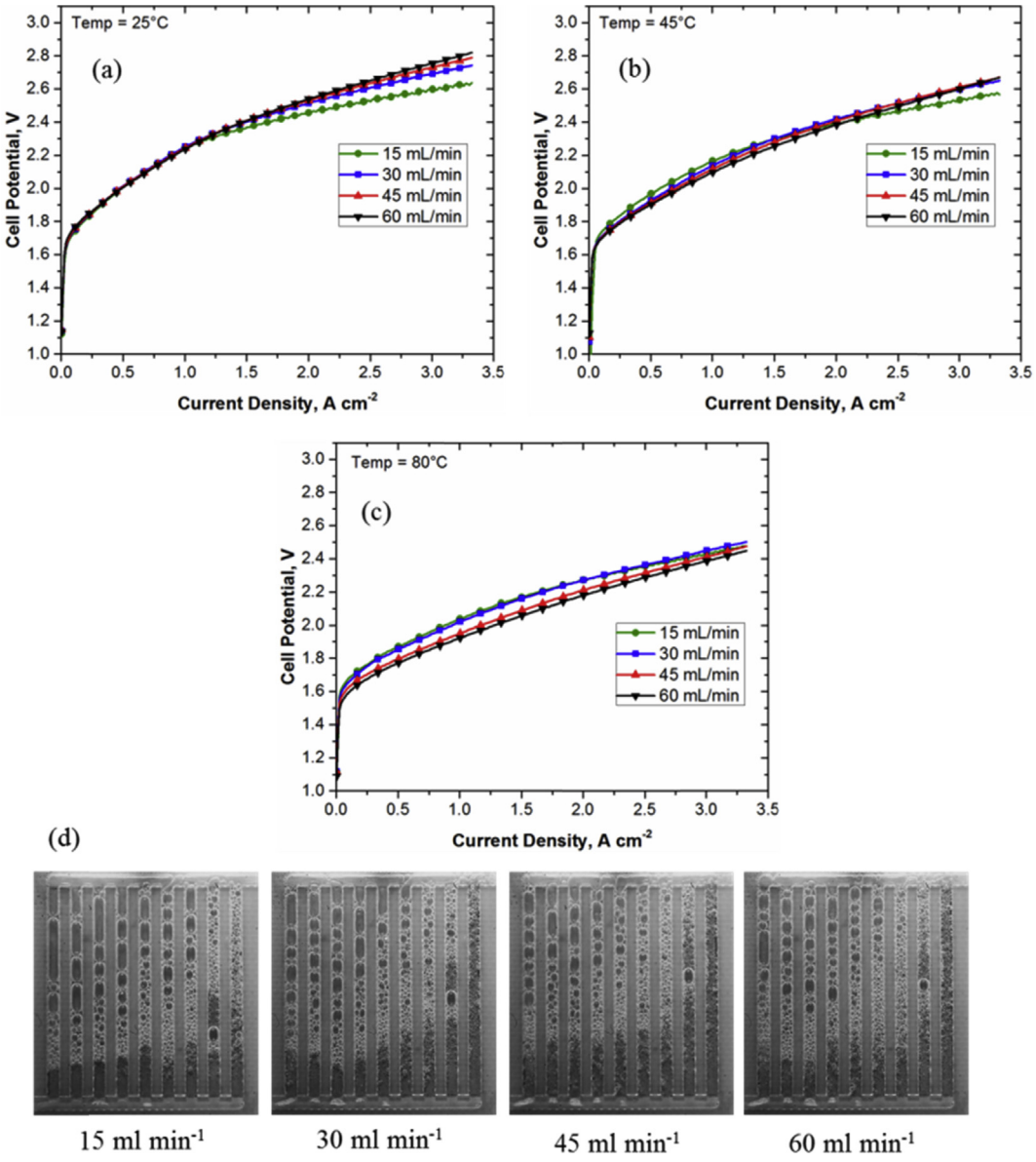

Fig. 8 – Effect of water flow rate on performance at different temperatures (a) 25 °C, (b) 45 °C, (c) 80 °C, (d) the two-phase flow behaviour under different anode flow rates at 2 A cm^{-2} and 80 °C using an anode-only circulation.

PFF design. More so, in terms of general trend, the flow velocity in the SSFF increased approximately linearly across the flow-field, while in relative terms there is hardly any velocity variation across the channels for the PFF. This difference in velocity is attributed to the fact that only a single meandering channel is present in the SSFF, whereas in the PFF the inlet flow is divided between the channels (nine, in this case). Since coalescence increases rapidly along the single channel length in SSFF, longer gas slugs are formed, and the flow velocity is noticeably higher in the upper part of the channel. Higher flow velocities have been reported to improve mass transfer in DMFCs [34,35]. However, the evidence presented here suggests that this is not the case in PEM electrolysers. Therefore, attention turns to the other key difference in the two-phase flow behaviour of these flow-field designs, which is the flow regime of operation. As discussed in Section General features of gas-bubble dynamics in the anode flow-field of the PEMWE, the bubble dynamics and two-phase flow regime differs markedly for the SSFF and PFF flow designs. In the SSFF, at a current density of 3.0 A cm^{-2}, a flow regime described as annular flow is observed, where continuous channel-filling gas slugs occupy the channel core with a thin layer of water flowing only at the walls.

In this situation, as depicted in the model in Fig. 6(d), it can be seen that the presence of long gas slugs spanning almost the entire length of the channel can block the access of water to the LGDL and lead to a deterioration in performance. This might explain why performance was worse in the SSFF, where continuous gas slugs spanning about 80% of the entire channel length can be found in the annular flow regime; whereas in the PFF, gas slugs formed towards the upper part of the channel rapidly exit into the combining manifold. Thus, in the

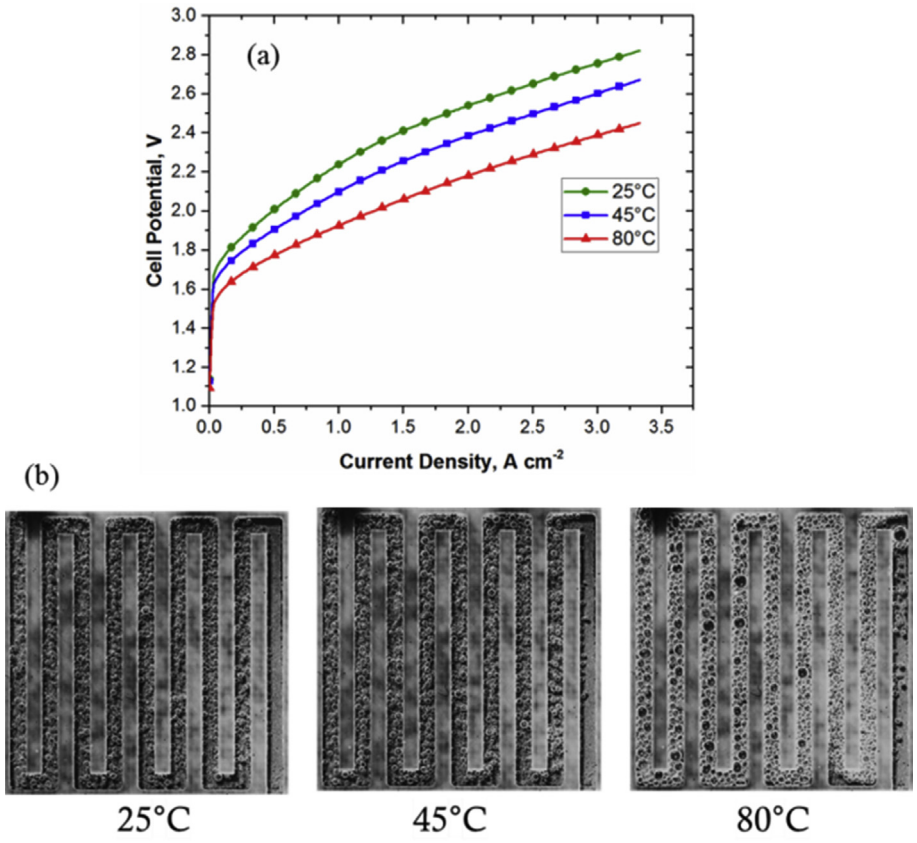

Fig. 9 – (a) Effect of temperature on PEMWE performance, (b) two-phase flow behaviour under different operating temperatures at a current density of 2 A cm^{-2} and water flow rate of 15 ml min^{-1}.

PFF, due to its short channel length, the discontinuous gas slugs formed are removed before they could develop into annular flow. Moreover, the effect of the fully developed gas slug in removing bubbles and clearing the channel, described by Dedigama et al. [22], is more pronounced in the PFF due to the shorter channel length. This observation, therefore, suggests that in terms of the two-phase flow behaviour in the PEMWE, the key performance-influencing difference between the SSFF and the PFF is the length of the flow path and hence the flow regime. The shorter flow path for gas removal in the PFF seems to enhance performance, and conversely, the elongated flow path of the SSFF allows gas accumulation and coalescence along the channel length that develops into annular flow that might hinder adequate water access to the electrocatalyst layer through the LGDL. Since the higher flow velocity in the SSFF did not lead to better performance, as predicted by similar DMFC research, it is inferred that the transition to annular flow regime exerts a higher impact than flow velocity on mass transport limitation and hence performance in PEMWEs.

Effect of operating conditions on the two-phase flow behaviour and cell performance

Effect of feed water circulation on cell performance

In PEMWE operation, water molecules accompany the transfer of protons from the anode to the cathode through the polymer electrolyte membrane, a phenomenon known as electroosmotic drag. Consequently, provided there is sufficient water at the anode, the membrane can be kept hydrated without an external supply of water to the cathode. However, water circulation at both electrodes is possible and is used in some commercial systems [46]. Thus, it is possible to operate with no water flow at the cathode (anode-only circulation), with stagnant water at the cathode, or with full water circulation at both cathode and anode. Fig. 7 presents the results of anode-only circulation and full circulation at both anode and cathode obtained at temperatures of 25 °C and 80 °C and water flow rates of 15 ml min^{-1} and 60 ml min^{-1} in the cell equipped with the PFF.

As can be seen in Fig. 7(a), at 25 °C, the full circulation showed worse performance than the anode-only circulation at both flow rates tested, the performance being worse at the higher flow rate. However, at 80 °C, (Fig. 7(b)), the cathode flow conditions shows little to no effect on the electrochemical performance at both flow rates tested, the performance being worse at the lower flow rate (in contrast to the 25 °C case). This is attributed to a thermal effect in which the Joule heating associated with operation at high current density has a beneficial effect on the proton conductivity of the membrane electrolyte. Both higher anode flow rate and additional cathode recirculation act to cool the cell. At 80 °C the cell is close to thermal equilibrium, and the flowing water does not have a cooling effect. Thus, full water circulation at this higher temperature has little to no impact on the cell performance.

Effect of water flow rate and temperature on two-phase flow and performance

The effect of anode water flow (15, 30, 45 and 60 mL min^{-1}) at a range of temperatures (25, 45 and 80 °C) was investigated (Fig. 8) using an anode-only water circulation.

It can be seen that the performance trend with increasing anode water flow rate changes from being deleterious at low temperature (25 °C) to advantageous at high temperature (80 °C), with relative insensitivity at intermediate temperature (45 °C). As described in Section Effect of feed water circulation on cell performance, water flow rate has a significant effect on performance at low water inlet temperature due to its cooling effect at higher current density when significant heat is being generated from the electrolyser. At the relatively high temperature of 80 °C, cell performance improves slightly with an increase in flow rates. This is attributed to the greater heat being supplied through the enthalpy of the higher flow water stream and ensures good reactant availability to the anode electrode. Also, from the two-phase flow perspective (Fig. 8(d)), the slug length is shortened with reduced residence time as water flow rate is increased from 15 ml min^{-1} to 60 ml min^{-1}. As a result, an increased effective contact area between inlet feed water and the LGDL enhance mass transfer leading to improved cell performance.

Effect of cell operating temperature on two-phase flow and performance

Fig. 9 shows the effect of temperature on PEMWE at a water flow rate of 15 ml min^{-1}. The experimental results indicate that cell performance improved with increasing temperature. At a current density of 3.0 A cm^{-2}, increasing the operating temperature from 25 °C to 80 °C resulted in a 242 mV improvement in cell potential. The improvement in performance with temperature can be explained by two reasons. First, at high temperatures, the activation overpotential is reduced, and the reaction kinetics is improved, which leads to an acceleration of the electrochemical reaction and improved performance. Also, the ohmic cell resistance is reduced at elevated temperatures since the ionic conductivity of the Nafion membrane (the largest contributor to ohmic resistance) is enhanced at high temperatures, provided sufficient membrane hydration can be ensured. This improvement in cell performance at high temperatures has been well reported [47–49]. Fig. 9(b) shows the effect of temperature on the two-phase flow at a current density of 2.0 A cm^{-2}. More gas bubbles are observed in the channels at higher inlet water temperature despite the same total current and amount of O_2 generated. This is attributed to the effect of temperature on the ideal gas law and fact that oxygen solubility in water is strongly temperature dependent and decreases at higher temperatures.

Conclusions

The two-phase flow behaviour in the anode flow channel of a PEMWE was investigated using optical visualization and related to the electrochemical performance for two commonly used flow-field designs. The effect of different operating parameters such as water circulation, water flow rate, and temperature on cell performance was also explored. The key findings of this study can be summarized as follows:

1. The flow-field design affects two-phase flow behaviour and hence, performance. The length of gas slugs and therefore the flow regime of operation is influenced by the path length of the flow-field channel.
2. The PFF yield better performance than the SSFF at high current densities under identical operating conditions which was attributed to the annular flow regime observed in the SSFF design where the channel-spanning long gas slugs formed hinders water access to the gas diffusion layer and electrocatalyst surface.
3. Higher water flow rate delays bubbly-to-slug transition and leads to the formation of smaller bubbles and shorter slugs.
4. The water flow rate effect on performance depends strongly on the cell operating temperature.

Acknowledgements

JOM gratefully acknowledges the Presidential Scholarship for Innovation and Development and Petroleum Technology Development Fund, Nigeria for supporting his research. DB and PRS acknowledge the EPSRC for supporting research in the Electrochemical Innovation Lab through (EP/M014371/1, EP/M023508/1, EP/M009394/1, EP/L015749/1, EP/K038656/1, EP/N022971/1).

REFERENCES

[1] Dunn S. Hydrogen futures: toward a sustainable energy system. Int J Hydrogen Energy 2002;27:235–64. https://doi.org/10.1016/S0360-3199(01)00131-8.
[2] Grigoriev SA, Porembsky VI, Fateev VN. Pure hydrogen production by PEM electrolysis for hydrogen energy. Int J Hydrogen Energy 2006;31:171–5. https://doi.org/10.1016/j.ijhydene.2005.04.038.
[3] Briguglio N, Andaloro L, Ferraro M, Di Blasi A, Dispenza G, Matteucci F, et al. Renewable energy for hydrogen production and sustainable urban mobility. Int J Hydrogen Energy 2010;35:9996–10003. https://doi.org/10.1016/j.ijhydene.2009.09.065.
[4] Smolinka T, Ojong ET, Garche J. Hydrogen production from renewable energies-electrolyzer technologies. Electrochem Energy Storage Renew Sources Grid Balancing 2014:103–28. https://doi.org/10.1016/B978-0-444-62616-5.00008-5.
[5] Barbir F. PEM electrolysis for production of hydrogen from renewable energy sources. Sol Energy 2005;78:661–9. https://doi.org/10.1016/j.solener.2004.09.003.
[6] Clarke RE, Giddey S, Ciacchi FT, Badwal SPS, Paul B, Andrews J. Direct coupling of an electrolyser to a solar PV system for generating hydrogen. Int J Hydrogen Energy 2009;34:2531–42. https://doi.org/10.1016/j.ijhydene.2009.01.053.
[7] Carmo M, Fritz DL, Mergel J, Stolten D. A comprehensive review on PEM water electrolysis. Int J Hydrogen Energy 2013;38:4901–34. https://doi.org/10.1016/j.ijhydene.2013.01.151.
[8] Ursùa A, Gandia LM, Sanchis P. Hydrogen production from water electrolysis: current status and future trends. Proc

IEEE 2012;100:410–26. https://doi.org/10.1109/JPROC.2011.2156750.
[9] Oi T, Sakaki Y. Optimum hydrogen generation capacity and current density of the PEM-type water electrolyzer operated only during the off-peak period of electricity demand. J Power Sources 2004;129:229–37. https://doi.org/10.1016/j.jpowsour.2003.11.050.
[10] Tunold R, Marshall AT, Rasten E, Tsypkin M, Owe L-E, Sunde S. Materials for electrocatalysis of oxygen evolution process in PEM water electrolysis cells. ECS Trans 2010;25:103–17. https://doi.org/10.1149/1.3328515.
[11] Grigoriev SA, Porembskiy VI, Korobtsev SV, Fateev VN, Auprêtre F, Millet P. High-pressure PEM water electrolysis and corresponding safety issues. Int J Hydrogen Energy 2011;36:2721–8. https://doi.org/10.1016/j.ijhydene.2010.03.058.
[12] Millet P, Ranjbari A, de Guglielmo F, Grigoriev SA, Auprêtre F. Cell failure mechanisms in PEM water electrolyzers. Int J Hydrogen Energy 2012;37:17478–87. https://doi.org/10.1016/j.ijhydene.2012.06.017.
[13] Ayers KE, Capuano C, Anderson EB. Recent advances in cell cost and efficiency for PEM-based water electrolysis. 2012. p. 15–22. https://doi.org/10.1149/1.3684798.
[14] Grigoriev SA, Dzhus KA, Bessarabov DG, Millet P. Failure of PEM water electrolysis cells: case study involving anode dissolution and membrane thinning. Int J Hydrogen Energy 2014;39:20440–6. https://doi.org/10.1016/j.ijhydene.2014.05.043.
[15] Sun S, Shao Z, Yu H, Li G, Yi B. Investigations on degradation of the long-term proton exchange membrane water electrolysis stack. J Power Sources 2014;267:515–20. https://doi.org/10.1016/j.jpowsour.2014.05.117.
[16] Gago AS, Ansar AS, Gazdzicki P, Wagner N, Arnold J, Friedrich KA. Low cost bipolar plates for large scale PEM electrolyzers. ECS Trans 2014;64:1039–48. https://doi.org/10.1149/06403.1039ecst.
[17] Lettenmeier P, Wang R, Abouatallah R, Helmly S, Morawietz T, Hiesgen R, et al. Durable membrane electrode assemblies for proton exchange membrane electrolyzer systems operating at high current densities. Electrochim Acta 2016;210:502–11. https://doi.org/10.1016/j.electacta.2016.04.164.
[18] Siracusano S, Baglio V, Van Dijk N, Merlo L, Aricò AS. Enhanced performance and durability of low catalyst loading PEM water electrolyser based on a short-side chain perfluorosulfonic ionomer. Appl Energy 2017;192:477–89. https://doi.org/10.1016/j.apenergy.2016.09.011.
[19] Van Der Merwe J, Uren K, Van Schoor G, Bessarabov D. Characterisation tools development for PEM electrolysers. Int J Hydrogen Energy 2014;39:14212–21. https://doi.org/10.1016/j.ijhydene.2014.02.096.
[20] Bertuccioli L, Chan A, Hart D, Lehner F, Madden B, Standen E. Study on development of water electrolysis in the EU. Final Report in Fuel Cells Hydrogen Joint Undertaking. 2014. Available online, https://www.fch.europa.eu/sites/default/files/study%20electrolyser_0-Logos_0_0.pdf.
[21] Ito H, Maeda T, Nakano A, Hasegawa Y, Yokoi N, Hwang CM, et al. Effect of flow regime of circulating water on a proton exchange membrane electrolyzer. Int J Hydrogen Energy 2010;35:9550–60. https://doi.org/10.1016/j.ijhydene.2010.06.103.
[22] Dedigama I, Angeli P, Ayers K, Robinson JB, Shearing PR, Tsaoulidis D, et al. In situ diagnostic techniques for characterisation of polymer electrolyte membrane water electrolysers - flow visualisation and electrochemical impedance spectroscopy. Int J Hydrogen Energy 2014;39:4468–82. https://doi.org/10.1016/j.ijhydene.2014.01.026.
[23] Dedigama I, Angeli P, Van Dijk N, Millichamp J, Tsaoulidis D, Shearing PR, et al. Current density mapping and optical flow visualisation of a polymer electrolyte membrane water electrolyser. J Power Sources 2014;265:97–103. https://doi.org/10.1016/j.jpowsour.2014.04.120.
[24] Sdeghi Lafmejani S, Olesen AC, Kær SK. Analysing gas-liquid flow in PEM electrolyser micro-channels. ECS Trans 2016;75:1121–7. https://doi.org/10.1149/07514.1121ecst.
[25] Selamet OF, Pasaogullari U, Spernjak D, Hussey DS, Jacobson DL, Mat MD. Two-phase flow in a proton exchange membrane electrolyzer visualized in situ by simultaneous neutron radiography and optical imaging. Int J Hydrogen Energy 2013;38:5823–35. https://doi.org/10.1016/j.ijhydene.2013.02.087.
[26] Hoeh MA, Arlt T, Kardjilov N, Manke I, Banhart J, Fritz DL, et al. In-Operando neutron radiography studies of polymer electrolyte membrane water electrolyzers. ECS Trans 2015;69:1135–40. https://doi.org/10.1149/06917.1135ecst.
[27] Hoeh MA, Arlt T, Manke I, Banhart J, Fritz DL, Maier W, et al. In operando synchrotron X-ray radiography studies of polymer electrolyte membrane water electrolyzers. Electrochem Commun 2015;55:55–9. https://doi.org/10.1016/j.elecom.2015.03.009.
[28] Nie J, Chen Y, Cohen S, Carter BD, Boehm RF. Numerical and experimental study of three-dimensional fluid flow in the bipolar plate of a PEM electrolysis cell. Int J Therm Sci 2009;48:1914–22.
[29] Tijani AS, Barr D, Rahim AHA. Computational modelling of the flow field of an electrolyzer system using CFD. Energy Procedia 2015;79:195–203. https://doi.org/10.1016/J.EGYPRO.2015.11.462.
[30] Aubras F, Deseure J, Kadjo J-JA, Dedigama I, Majasan J, Grondin-Perez B, et al. Two-dimensional model of low-pressure PEM electrolyser: two-phase flow regime, electrochemical modelling and experimental validation. Int J Hydrogen Energy 2017;42:26203–16. https://doi.org/10.1016/j.ijhydene.2017.08.211.
[31] Ruiz DDH, Sasmito AP, Shamim T. Numerical investigation of the high temperature PEM electrolyzer: effect of flow channel configurations. ECS Trans 2013;58:99–112. https://doi.org/10.1149/05802.0099ecst.
[32] Toghyani S, Afshari E, Baniasadi E, Atyabi SA. Thermal and electrochemical analysis of different flow field patterns in a PEM electrolyzer. Electrochim Acta 2018;267:234–45. https://doi.org/10.1016/J.ELECTACTA.2018.02.078.
[33] Kamarudin SK, Achmad F, Daud WRW. Overview on the application of direct methanol fuel cell (DMFC) for portable electronic devices. Int J Hydrogen Energy 2009;34:6902–16. https://doi.org/10.1016/j.ijhydene.2009.06.013.
[34] Arico AS, Creti P, Baglio V, Modica E, Antonucci V. Influence of flow field design on the performance of a direct methanol fuel cell. J Power Sources 2000;91:202–9.
[35] Oliveira VB, Rangel CM, Pinto AMFR. Effect of anode and cathode flow field design on the performance of a direct methanol fuel cell. Chem Eng J 2010;157:174–80. https://doi.org/10.1016/j.cej.2009.11.033.
[36] Scott K, Taama W, Argyropoulos P. Material aspects of the liquid feed direct methanol fuel cell. J Appl Electrochem 1998;28:1389–97.
[37] Tüber K, Oedegaard A, Hermann M, Hebling C. Investigation of fractal flow-fields in portable proton exchange membrane and direct methanol fuel cells. J Power Sources 2004;131:175–81. https://doi.org/10.1016/j.jpowsour.2003.11.078.
[38] Argyropoulos P, Scott K, Taama W. Carbon dioxide evolution patterns in direct methanol fuel cells. Electrochim Acta 1999;44:3575–84. https://doi.org/10.1016/S0013-4686(99)00102-4.

[39] Hwang SY, Joh HI, Scibioh MA, Lee SY, Kim SK, Lee TG, et al. Impact of cathode channel depth on performance of direct methanol fuel cells. J Power Sources 2008;183:226–31. https://doi.org/10.1016/j.jpowsour.2008.04.043.
[40] Yang H, Zhao TS, Ye Q. In situ visualization study of CO2 gas bubble behavior in DMFC anode flow fields. J Power Sources 2005;139:79–90. https://doi.org/10.1016/j.jpowsour.2004.05.033.
[41] Vijayakumar R, Rajkumar M, Sridhar P, Pitchumani S. Effect of anode and cathode flow field depths on the performance of liquid feed direct methanol fuel cells (DMFCs). J Appl Electrochem 2012;42:319–24. https://doi.org/10.1007/s10800-012-0396-2.
[42] Liao Q, Zhu X, Zheng X, Ding Y. Visualization study on the dynamics of CO2 bubbles in anode channels and performance of a DMFC. J Power Sources 2007;171:644–51. https://doi.org/10.1016/j.jpowsour.2007.06.257.
[43] Wong CW, Zhao TS, Ye Q, Liu JG. Transient capillary blocking in the flow field of a micro-DMFC and its effect on cell performance. J Electrochem Soc 2005;152:A1600. https://doi.org/10.1149/1.1949067.
[44] Yuan W, Wang A, Yan Z, Tan Z, Tang Y, Xia H. Visualization of two-phase flow and temperature characteristics of an active liquid-feed direct methanol fuel cell with diverse flow fields. Appl Energy 2016;179:85–98. https://doi.org/10.1016/j.apenergy.2016.06.127.
[45] Wang J. Theory and practice of flow field designs for fuel cell scaling-up: a critical review. Appl Energy 2015;157:640–63. https://doi.org/10.1016/j.apenergy.2015.01.032.
[46] Butterworth D, Hewitt GF. Two-phase flow and heat transfer. 1977.
[47] Selamet ÖF, Becerikli F, Mat MD, Kaplan Y. Development and testing of a highly efficient proton exchange membrane (PEM) electrolyzer stack. Int J Hydrogen Energy 2011;36:11480–7. https://doi.org/10.1016/j.ijhydene.2011.01.129.
[48] Awasthi A, Scott K, Basu S. Dynamic modeling and simulation of a proton exchange membrane electrolyzer for hydrogen production. Int J Hydrogen Energy 2011;36:14779–86. https://doi.org/10.1016/j.ijhydene.2011.03.045.
[49] Xu W, Scott K, Basu S. Performance of a high temperature polymer electrolyte membrane water electrolyser. J Power Sources 2011;196:8918–24. https://doi.org/10.1016/j.jpowsour.2010.12.039.